Exploring the Signal Content of Continuous Seismic Recordings at Station NKC (West-Bohemia/Vogtland) With a Self-Supervised Vision Transformer

Non-peer reviewed preprint submitted to EarthArXiv

Marcel van Laaten[1], Roman Esefelder[1]

[1]Institute of Geosciences, Friedrich Schiller University Jena, Burgweg 11, 07749 Jena, Germany

Key Points:

- A DINOv3 vision transformer learns a representation of spectrograms directly from unlabelled, STA/LTA-triggered windows at station NKC.
- Unsupervised clustering recovers earthquake-enriched groups that track the known swarm episodes and separate P- from Lg-dominated windows.
- Most triggered windows have no catalogue counterpart.

Corresponding author: Marcel van Laaten, `marcel.vanlaaten@uni-jena.de`

Abstract

Continuous seismic recordings contain a wide variety of signal types (earthquakes, quarry blasts, induced events, and diverse background and anthropogenic noise) but sorting them into meaningful categories usually relies on manual inspection. Here we take an exploratory approach and ask a deliberately simple question: what kinds of signals are actually present in the continuous record of station NKC, and can we let the data organise themselves without imposing labels beforehand? Station NKC lies in the West-Bohemia/Vogtland earthquake swarm region and records a mixture of earthquakes and non-earthquake transients. We select waveform windows with an STA/LTA trigger, represent each window as a continuous-wavelet-transform spectrogram of all three components, and use a self-supervised vision transformer (DINOv3) to group the windows by similarity. Because the model learns its representation directly from the unlabelled spectrograms, the resulting structure reflects the data rather than a predefined catalogue. We then examine the groups that emerge and compare them, where possible, against earthquake catalogues and against the waveforms themselves. The learned representation separates earthquakes clearly from the background, and unsupervised clustering recovers groups that are strongly enriched in earthquakes and that concentrate in the known swarm episodes. Equally informative is what the clustering reveals about the rest of the record. A large fraction of triggered windows have no catalogue counterpart, and inspection shows that many of these are themselves earthquake-like signals. We present the signal groups identified and discuss their likely physical interpretation.

Plain Language Summary

Seismometers record ground motion continuously, and their recordings mix many kinds of signals: small earthquakes, blasts from quarries, machinery, weather-related shaking, and background noise. Deciding which recording belongs to which category is slow work, and the earthquake catalogues used as a reference are known to miss events. We tested whether a computer can sort these signals on its own, without being told the categories in advance. Using recordings from a station in the West-Bohemia/Vogtland region, an area known for earthquake swarms, we turned short windows of ground motion into images that show how their energy is distributed in time and frequency, and let a modern self-supervised learning model group similar images together. The model cleanly separated earthquakes from other signals and rediscovered the timing of the known earthquake swarms. It also revealed that many earthquake-like signals in the record were never listed in the catalogue, which suggests that this kind of data-driven exploration could help build more complete catalogues in the future.

1 Introduction

Continuous seismic recordings are a rich but awkward data source. A single broadband station registers earthquakes of every size, quarry blasts, induced events, machinery, traffic, weather-driven ground motion, and a floor of background noise, all interleaved and often overlapping. Turning this stream into something usable has traditionally meant one of two things: manual inspection by an analyst, or automatic detection followed by classification. Both are effective, and both are limited. Manual inspection does not scale to years of data, and detection-based catalogues carry the biases of the detector and of the templates or labels used to build them. As a result, the catalogues that seismologists rely on as ground truth are known to be incomplete, particularly for small or unusual events (Rimpot, Hibert, Malet, et al., 2025).
Machine learning, and deep learning in particular, has become a standard tool for classifying seismic signals from their time–frequency representations. Convolutional neural networks and, more recently, vision transformers achieve high accuracy at discriminating event types when trained on labelled spectrograms. In the very region we study here,

Kasburg et al. (2025) discriminated earthquakes along the Leipzig-Regensburg fault zone from quarry blasts with accuracies of 97-98% using both a CNN baseline and vision transformers. These supervised approaches are powerful, but they share two structural constraints. First, they require labels, and the quality of the result is bounded by the quality of the labelling. Second, because the labels come from catalogues, a supervised model can only learn the categories the catalogue already contains. Signals that were never catalogued are, by design, invisible to it.
Self-supervised learning (SSL) offers a different starting point. Rather than mapping spectrograms to predefined labels, an SSL model learns a representation of the data from the data alone, so the structure it discovers reflects what is actually present in the record.
Recent seismological applications are encouraging. Rimpot, Hibert, Retailleau, et al. (2025) applied a Siamese network (SimSiam) to spectrogram images of continuous recordings at the Mayotte submarine volcano and, through clustering of the learned representation, recovered previously undocumented eruptive sequences that would have been difficult to see in the raw traces. Rimpot, Hibert, Malet, et al. (2025) scaled a related workflow (using BYOL, k-means, and agglomerative clustering) to more than ten million windows from a dense array, and organised a landslide data set into coherent families of noise, rainfall-induced signals, and endogenous seismic events. Both studies emphasise two points that motivate the present work: SSL clustering can surface rare and uncatalogued signals, and the resulting clusters are informative even when they are not perfectly pure.
What has not yet been tried, to our knowledge, is the combination of a modern self-distillation vision transformer of the DINO family (Caron et al., 2021) with an exploratory analysis of a earthquake swarm station, where natural seismicity and a busy background of anthropogenic and ambient transients coexist. This is the setting we address. We apply a DINOv3 like vision transformer (Siméoni et al., 2025) to continuous-wavelet-transform (CWT) spectrograms of STA/LTA-triggered windows at station NKC and ask what the continuous record contains, letting the data self-organise before we attach any interpretation.
The goal is to explore and organise the data, not to achieve a high degree of accuracy in classification. A supervised discriminator, given clean labels, will out-perform an unsupervised representation at the narrow task of ranking earthquakes ahead of everything else, and a simple pixel space baseline is a strong competitor at sharp retrieval precision (Section 3.5). The value we see in the self-supervised approach lies elsewhere: in producing an unsupervised taxonomy of signal types, in separating physically distinct sources without being told they are distinct, and in exposing where the catalogue is incomplete.

2 Data

2.1 Station NKC and the West-Bohemia/Vogtland swarm region

Station NKC (Nový Kostel) sits in the West-Bohemia/Vogtland region on the Czech–German border (Fig. 1). The seismicity forms a dense, roughly north–south trending cloud centred on the station, embedded in a wider field of more diffuse activity. The swarms are widely interpreted as fluid-driven, associated with the ascent of mantle-derived volatiles through the crust (Fischer et al., 2014; van Laaten et al., 2023). The region has been the subject of extensive seismological studies (Hrubcová et al., 2005; Fischer et al., 2014; Heinicke et al., 2019; van Laaten & Wegler, 2024; Büyükakpinar et al., 2026). For our purposes the important property is simply that NKC records a large number of genuine earthquakes alongside a busy background of quarry blasts, machinery, and weather-related transients, which makes it a natural testbed for an exploratory analysis of signal content.

2.2 Data and catalogue

We use the three continuous broadband components (HHZ, HHN, HHE) of station NKC (Charles University in Prague et al., 1973) over the period 2016 - 2024 and filtered between 0.5 - 25 Hz. To concentrate the analysis on signal-bearing windows, we ran an STA/LTA trigger (Allen, 1982) on the continuous record with an STA window length of 1 s, 60 s for LTA and trigger threshold of 4.5 and extracted 30 s windows around each trigger (5 s pre and 25 post-trigger). This yields approximately 198,000 windows in total, of which around 171,000 are STA/LTA triggers. Whenever the STA/LTA trigger did not fire, the segment had a 5% chance of being included in the dataset, resulting in approximately 27,000 additional, untriggered windows being retained to represent the background noise (Fig. 2). Working on the triggered subset rather than reducing the noise fraction during preprocessing is functionally equivalent but computationally cleaner: it puts the model's capacity where the signals are.

For evaluation and interpretation only, not for training, we matched the triggered windows against the regional TSN bulletin (Institut fuer Geowissenschaften, Friedrich-Schiller-Universitaet Jena, 2009), keeping catalogued events within 40 km of NKC. Each window is thereby assigned one of three reference labels: earthquake (a catalogue earthquake falls in the window), noise (a manually flagged background window), or triggered unmatched (the window triggered the detector but has no catalogue counterpart). We stress that these labels are imperfect. In our experience only the earthquake labels are reliable enough to support quantitative evaluation. The triggered unmatched category, in particular, is not a signal class but simply the residue of everything the catalogue did not capture, and a substantial part of it turns out to be earthquake-like (Section 4.6).

3 Method

3.1 From waveforms to spectrogram images

The processing pipeline is summarised in Fig. 2. Each 30 s, three-component window is transformed into a time–frequency image with the CWT, computed independently for HHZ, HHN, and HHE. The three component scalograms are stacked into a three-channel image analogous to the RGB channels of a natural image, resized to 192 × 192 pixels, and quantised to 8-bit, keeping all three components as separate channels rather than collapsing to a single trace.

Next we normalise the amplitude. We convert the CWT amplitude to decibels ($20 \log_{10}$) and then apply a hyperbolic-tangent saturation with scale factor 3.0 before quantisation. We adopted this after finding that a per-window percentile normalisation, rescaling each spectrogram to its own dynamic range, makes noise and earthquake spectrograms look nearly identical to the model, because it discards precisely the amplitude contrast that distinguishes an energetic arrival from a quiet background. The decibel scaling preserves relative energy, and the tanh saturation prevents a few extreme values from dominating the 8-bit range.

3.2 Self-supervised representation learning

We learn the representation with a DINOv3 vision transformer (small variant, patch size 8, input 192 × 192, embedding dimension 384). The transformer architecture and its application to images follow Vaswani et al. (2017) and Dosovitskiy et al. (2020). The self-supervised objective is the DINO self-distillation scheme (Caron et al., 2021), in which a student network is trained to match the output of an exponential-moving-average teacher across two augmented views of the same window, combined with the iBOT masked-patch prediction objective (Zhou et al., 2021). We use the stabilising ingredients introduced with DINOv2 (Oquab et al., 2024), the KoLeo regulariser, which encourages the embeddings to spread out and discourages collapse, together with Sinkhorn–Knopp centering of the teacher assignments, and the additional components of the DINOv3 recipe, namely rotary positional embeddings (RoPE) and register tokens.

Our data augmentation departs deliberately from the transformations common in generic image SSL. We use energy-weighted temporal cropping (so that crops preferentially con-

tain the energetic part of the window) and time-only crops. We do not use time reversal, frequency-axis flips, colour jitter, or solarisation, because none of these preserves the physical meaning of a seismic spectrogram. The frequency axis carries source and path information, and the causal time structure of a phase arrival is not invariant under reversal. This is a conscious difference from (Rimpot, Hibert, Retailleau, et al., 2025), who applied flips and colour changes on the argument that a flipped spectrogram remains interpretable. For a swarm setting in which the distinction between phases and frequency content is exactly what we hope to learn, we prefer to keep the frequency axis intact.
Training used four A100 GPUs with distributed data-parallel (torchrun) with 170 epochs trained. We selected the checkpoint used for all downstream analysis by its downstream retrieval performance (Section 3.4), not by the training loss. This choice is deliberate: in DINO training the loss commonly continues to drift upward after the representation has matured, because the moving-average teacher produces progressively harder targets. The post-peak loss rise is a normal feature of the optimisation rather than a sign of overfitting, and using it for model selection would be misleading.

3.3 Clustering and visualisation

From the trained encoder we extract the CLS-token embedding of each window, giving a matrix of 198,000 × 384. For visualisation we reduce this to two dimensions with UMAP (McInnes et al., 2020), fitting the projection on a subset and transforming the full set so that the embedding scale is handled consistently. UMAP is used for display only. All quantitative analysis is performed in the full 384-dimensional space.
For clustering we apply the Leiden algorithm (Traag et al., 2019) to a nearest-neighbour graph built in the embedding space, using the RBConfiguration objective, a cosine metric, and resolution 2.0. This produces 32 clusters. We then group the 32 clusters into eight macro-classes by inspecting their feature-deviation signatures (Section 3.4) together with label-free metadata (weekday, hour, dominant frequency, trigger duration, catalogue distance where available), cross-referenced against catalogue statistics. The macro-classes and their sizes are summarised in Tab. 1.

3.4 Evaluation and cluster interpretation

Because only the earthquake labels are reliable, we evaluate the representation with a retrieval metric restricted to those labels. For an earthquake-labelled query window q, let $N_k(q)$ be its k nearest neighbours in embedding space under cosine distance. Precision-at-k is

$$P@k(q) = \frac{1}{k} \sum_{n \in N_k(q)} 1\,[\text{label}(n) = \text{earthquake}] \tag{1}$$

and we report the mean over all earthquake queries. P@k measures how strongly earthquakes cluster with earthquakes in the learned space, without requiring reliable labels for any other class.
As a stability and collapse diagnostic we use the effective rank of the embedding (Roy & Vetterli, 2007). With $\sigma_1 \geq \cdots \geq \sigma_d$ the singular values of the (centred) embedding matrix and $p_i = \sigma_i / \sum_j \sigma_j$

$$\text{erank} = \exp\left(-\sum_i p_i \ln p_i\right) \tag{2}$$

which ranges from 1 (all variance in one direction, total collapse) to $d = 384$ (variance spread evenly). We prefer the effective rank to a fixed-threshold collapse monitor because it is scale-invariant and gives a continuous, interpretable measure of how many dimensions the representation actually uses.
To interpret individual clusters we use a feature-deviation signature. For each cluster we compute the mean patch-token feature deviation relative to the global distribution and map it back onto the time–frequency plane of the input, which highlights where in

the spectrogram a cluster differs most from the rest of the data. We summarise each cluster by the maximum of this signature, $\mathrm{Characteristic}_{\mathrm{max}}$ (Section 4.4).

3.5 A pixel-space baseline, and honest framing

To put the learned representation in context we compare it against a simple baseline: principal-component analysis of the raw spectrogram pixels followed by k-nearest-neighbour retrieval (pixel-PCA-kNN). The comparison is instructive and we report it plainly. The pixel baseline out-performs the self-supervised representation at sharp retrieval precision (k in the range 20–100), whereas the self-supervised representation wins at tail recall ($k \geq 500$). In other words, a linear method on raw pixels is already good at finding an earthquake's nearest look-alikes, and the deep representation's advantage is in recovering the broader, more diffuse population of related events. This is consistent with our overall position: the contribution of the self-supervised model is not to maximise retrieval precision but to organise the record into coherent, physically interpretable groups.

4 Results

4.1 Training behaviour

Training converges to a stable representation without collapse (Fig. 3). The earthquake retrieval precision P@20 improves over training and plateaus near 0.82, roughly 2.8 times the level of about 0.29 expected for random retrieval, with most of the gain achieved by epoch 100. In parallel, the effective rank rises monotonically from about 90 to about 305 out of 384 and shows no sign of the decline that would accompany representational collapse. The two curves rising together, retrieval quality and effective dimensionality, indicate that the model is spreading the windows across many directions of the embedding while still placing earthquakes near earthquakes. As noted in Section 3.2, the training loss continued to drift after this point. The downstream metrics, not the loss, guided checkpoint selection.

4.2 Macro-structure of the learned representation

The two-dimensional UMAP projections give a first, qualitative view of the representation (Fig. 4). Coloured by cluster (Fig. 4a), the embedding resolves into a large number of contiguous regions rather than a single undifferentiated mass. Coloured by time (Fig. 4b), several regions are clearly time localised. A reminder that the representation captures episodic regimes such as earthquake swarms and data-quality episodes, not only signal morphology. Most directly, when the catalogue earthquakes ($n = 5{,}866$ windows) are highlighted (Fig. 4c), they occupy a coherent, well-delimited part of the map and are cleanly separated from the bulk of the record. The representation therefore learns an earthquake/background distinction without ever being shown the labels. The same embedding, coloured by the eight macro-classes of our taxonomy (Fig. 5), shows that each class occupies a distinct territory. The ambient-transient class is by far the largest single population (about 102,000 windows), forming the central bulk of the map, while earthquakes (about 21,000), quarry blasts (about 30,000), and the smaller classes (noise, instrument/machinery, artifact/episode, teleseismic, and a mixed/ambiguous class) form their own regions around and within it. The counts for all eight classes are given in Tab. 1 and example spectrograms of the various macro-classes are shown in Fig. 6.

4.3 Cluster sizes and catalogue composition

Fig. 7 shows the 32 Leiden clusters ordered by size (Fig. 7a) and their composition in terms of the three reference labels (Fig. 7b). The clusters range from roughly 13,000 windows down to a few hundred. A handful are dominated by their catalogue labels in

a way that makes their identity clear. Several clusters are noise-dominated (for example C3, C29, and C30, with noise fractions of 83%, 86%, and 95%), and the earthquake enrichment concentrates in a small number of clusters (for example C23, with 36% catalogue-earthquake windows, and C7, C9, and C17 with 14-21%).
The dominant feature of Fig. Fig. 7b, however, is the triggered unmatched row. In the large majority of clusters, the triggered unmatched fraction is between 80% and 100%. This is not a statement about signal morphology, it is a statement about the catalogue. Most windows that triggered the detector, including most windows in the clusters we identify as earthquakes, have no catalogue counterpart. We return to what this implies in Section 4.6.

4.4 What the clusters are: feature-deviation signatures

The feature-deviation signatures make the physical identity of the distinctive clusters legible (Fig. 8). Representative signatures include a sharp, monochromatic line near 15 Hz (C30, an instrument/machinery line), a broadband, low-frequency-enriched pattern (C31, teleseismic), the characteristic time–frequency shape of a quarry blast (C8), a long-duration high-frequency signature consistent with machinery or traffic (C16), and two earthquake signatures dominated by different phases (C25 and C27). A short-duration, high-amplitude glitch pattern (C18) corresponds to the artifact/episode class.
The bar chart of $\text{Characteristic}_{\text{max}}$ across all 32 clusters (Fig. 8, bottom) quantifies this and also exposes a limitation. The physically distinct clusters (instrument, teleseismic, earthquake, quarry blast, machinery, artifact) have high $\text{Characteristic}_{\text{max}}$ (roughly 12–23), reflecting spectrograms that deviate strongly and consistently from the global average. The many clusters that make up the ambient-transient bulk have low $\text{Characteristic}_{\text{max}}$ (roughly 7–9). We read this as evidence that the transient bulk is over-fragmented: the clustering splits a large, internally similar population into many neighbouring clusters that are not individually distinctive, while the genuinely distinct signal types form well-separated, high-deviation clusters. The feature-deviation signature thus provides an independent, label-free confirmation of which parts of the taxonomy are meaningful and which are artefacts of the clustering resolution.

4.5 Temporal fingerprints and phase sub-structure

Two temporal analyses corroborate the taxonomy without using catalogue labels. The monthly window counts per macro-class (Fig. 9) show that the earthquake class peaks in a small number of episodes, most prominently around 2018, with further episodes around 2021 and 2024, coinciding with the documented swarm activity of the region. The artifact/episode class is concentrated almost entirely in a single 2023 data-quality episode. The quarry-blast and ambient-transient classes, by contrast, are present throughout the record.
The weekday and hour-of-day distributions (Fig. 10) sharpen the interpretation. Quarry blasts are strongly concentrated on working days (Monday–Friday) and peak around local midday, the classic signature of controlled surface blasting. Earthquakes are essentially flat across weekdays and hours, as expected for a natural process. The ambient-transient and noise classes are elevated at weekends, and the machinery/instrument class peaks on weekdays around midday. Because these patterns are computed from time stamps alone, they provide independent support for the physical labels we attach to the macro-classes.
Finally, the representation resolves structure within the earthquake population. Fig. 11 focuses on two earthquake-associated clusters, C25 and C27, associating each of their windows with the nearest catalogued origin and plotting the delay between origin time and window onset against catalogued epicentral distance. The two clusters fall on distinct travel-time branches: C25 follows a fast branch consistent with the first-arriving P/Pn phase (apparent velocities of roughly 6–8 km/s, median near 6.7 km/s), while C27

follows a slow branch consistent with the Lg phase (near 3.4 km/s). In other words, the self-supervised representation separates earthquake windows according to which seismic phase dominates the 30 s window, a physically meaningful distinction that reflects source–receiver distance and the moveout of phases, and that the model was never asked to make. The teleseismic cluster C31 is the end-member of this behaviour: its windows are consistent with a very distant, large earthquake recorded at long range (on the order of 1000 km) with a Pn-type apparent velocity, which is why it separates so cleanly from the local seismicity.

4.6 Triggered detections without a catalogue counterpart

The single most consequential result is quantitative and follows directly from the comparison in the previous sections. Our taxonomy assigns about 21,000 windows to the earthquake class (Tab. 1), whereas only about 5,900 windows are matched to a catalogued earthquake (Fig. 4c). The difference, roughly 15,000 windows, is dominated by triggered unmatched windows that nevertheless fall inside earthquake clusters, share the earthquake feature-deviation signatures, and, on manual inspection of a sample, show earthquake-like waveforms. We are deliberately cautious in interpreting this excess. The regional bulletin is comparatively complete for tectonic events in this densely monitored area, so reading the excess as missing earthquakes alone would be unwarranted. Earthquake-like morphology does not by itself establish a tectonic origin: the region hosts active quarries, and regional blasts can produce impulsive, earthquake-like signals that require dedicated analysis to separate from natural events (Kasburg et al., 2025). The taxonomy does resolve a distinct quarry-blast class (Tab. 1), but unsupervised clustering on morphology need not separate every blast from every earthquake, and blasts that resemble earthquakes can fall in earthquake clusters. A more defensible reading is therefore that these approx. 15,000 windows are a mixed population of morphologically earthquake-like signals, sub-threshold or otherwise uncatalogued earthquakes together with quarry blasts and other transients, that the detector captured but the catalogue does not resolve.

The value of the result does not depend on resolving this ambiguity. What the clustering does is bring the uncatalogued population to the surface in an organised way, grouped with catalogued earthquakes by morphology, not scattered at random. Thereby turn a diffuse set of unclassified triggered detections into a concrete, reviewable candidate list whose composition can be settled by targeted follow-up (for example, relocation for the earthquake candidates, or timing- and spectral-based discrimination for the blast candidates). This is the kind of use for which the exploratory, unsupervised approach is well suited, and it is not available to a supervised classifier trained on the catalogue.

5 Discussion

5.1 What the self-supervised approach contributes

The results support a specific reading of what SSL adds in this setting. It does three things that a supervised discriminator does not. It produces a label-free taxonomy of signal types, grouping the record into earthquakes, blasts, teleseismic, machinery, ambient transients, noise, and a data-quality episode. It recovers physically meaningful substructure, the separation of P- and Lg-dominated earthquake windows (Fig. 11) is the clearest example, without being told those distinctions exist. And it surfaces a large population of triggered detections that the catalogue does not resolve, in an actionable form (Section 4.6). These are the same broad strengths that earlier SSL clustering studies reported in volcanic and glacial settings (Rimpot, Hibert, Retailleau, et al., 2025; Rimpot, Hibert, Malet, et al., 2025; Jiang et al., 2026), now demonstrated in a earthquake swarm context with a modern self-distillation transformer.

It is worth placing this next to the supervised work in the same region. Kasburg et al. (2025) showed that, with clean labels, earthquakes and quarry blasts can be discriminated at 97–98% accuracy. That is a genuinely higher performance at the specific task of classification, and we do not compete with it. The two approaches are complementary: supervised discrimination answers which of these known categories does this window belong to, while the exploration here answers what categories are in the record at all, and what is the catalogue missing. A natural workflow uses the second to inform and audit the first.

5.2 Limitations

Several limitations bound the interpretation. The clearest, discussed in Section 4.4, is the over-fragmentation of the ambient-transient bulk: at resolution 2.0 the Leiden clustering splits a large, internally similar population into many low-deviation clusters. A single global resolution cannot be optimal for both the compact, distinctive classes and the diffuse ambient population. An iterative or hierarchical refinement, such as that used by Rimpot, Hibert, Malet, et al. (2025), in which a coarse pass isolates the ambient bulk and a second pass re-clusters it at higher resolution, is a natural next step and would likely improve the resolution of weather-driven sub-types. We see, for instance, candidate rainfall- and storm-related clusters within the ambient class, but do not resolve them cleanly here.

The catalogue is an imperfect ground truth, and this is the binding constraint on quantitative evaluation. Only the earthquake labels are reliable enough to use, which is why we restrict the retrieval metric to them and treat the triggered unmatched category as a residue rather than a class. The result in Section 4.6 is suggestive but rests on manual inspection of a sample. Resolving the origin of the uncatalogued earthquake-class windows at scale, separating sub-threshold earthquakes from quarry blasts and other transients, would require dedicated relocation, discrimination, or template-matching analysis, which is beyond the scope of this exploratory study.

The analysis is single-station. Much of the physical sub-structure we recover, most obviously the P/Lg phase separation, is expressible at a single station, and a single station is the natural unit for a first exploratory study. Extending the representation to multiple stations, so that spatial coherence between stations can be exploited, is a clear avenue for future work and would help distinguish co-located sources that a single station cannot separate.

Finally, our augmentation choices reflect a judgement, not a proven optimum. We kept the frequency axis and the causal time structure intact, on the argument that they carry the very information we want the model to use. Rimpot, Hibert, Retailleau, et al. (2025) made the opposite choice and used flips and colour jitter successfully. A systematic study of which augmentations preserve or destroy seismically meaningful invariances would be valuable and is, as far as we know, still open.

6 Conclusions

We applied a self-supervised vision transformer of the DINO family to continuous-wavelet spectrograms of STA/LTA-triggered windows at the West-Bohemia/Vogtland swarm station NKC, with the deliberately exploratory aim of asking what the continuous record contains, without imposing labels beforehand. The learned representation, trained on unlabelled spectrograms, cleanly separates earthquakes from the background and organises the record into an eight-class taxonomy of signal types. Unsupervised clustering recovers groups that are strongly enriched in earthquakes and that concentrate in the documented swarm episodes. It distinguishes anthropogenic quarry blasts, which cluster on working days around midday, from natural earthquakes, which are flat in time; and it resolves physically meaningful sub-structure within the earthquake population, separating P- from Lg-dominated windows along their travel-time branches.

The result we regard as most consequential concerns the catalogue rather than the model. The taxonomy places about 21,000 windows in the earthquake class, while only about 5,900 are matched to a catalogued earthquake, leaving roughly 15,000 triggered windows that share earthquake morphology yet have no catalogue counterpart. In a region whose bulletin is comparatively complete for tectonic events, this population is most plausibly mixed, sub-threshold earthquakes together with quarry blasts and other transients, rather than missing earthquakes alone, and its composition is an open question for targeted follow-up. Self-supervised exploration surfaces this population in an organised, reviewable form. We therefore see the approach less as a competitor to supervised discrimination, which remains more accurate at classifying known categories, than as a complement to it: a way to discover what is in a continuous record and to flag detections that the catalogue does not resolve.

Open Research Section

The station NKC is part of the CZ network (Charles University in Prague et al., 1973). The seismic waveform data are openly available and can be downloaded from the IRIS Data Centre `https://service.earthscope.org/fdsnws/dataselect/docs/1/builder/`. The local earthquake bulletin and regional earthquake bulletin is open available and can be downloaded from the TSN `https://www.erdbebenwahrnehmung-thueringen.uni-jena.de/aktuelle_Ereignisse/Bulletin_archiv.txt` and EMSC `https://seismicportal.eu/fdsn-wsevent.html` respectively. The topographic data used in this study were obtained from the Global Multi-Resolution Topography (GMRT) synthesis (Ryan et al., 2009), accessible via `https://www.gmrt.org/GMRTMapTool/`. All analyses and figures were generated using the open-source Python packages: Cartopy (`https://cartopy.readthedocs.io`), Matplotlib (`https://matplotlib.org/`), NumPy (`https://numpy.org/`), ObsPy (`https://docs.obspy.org/`), pandas (`https://pandas.pydata.org/`), pytorch (`https://pytorch.org/`), scikit-learn (`https://scikit-learn.org`), and SciPy (`https://scipy.org/`).

Conflict of Interest declaration

The author declares that there are no conflicts of interest for this manuscript.

Acknowledgments

References

Allen, R. (1982). Automatic phase pickers: Their present use and future prospects. *Bulletin of the Seismological Society of America*, *72*(6B), S225-S242. doi: 10.1785/BSSA07206B0225

Büyükakpinar, P., Dahm, T., Isken, M., Doubravová, J., Kriziová, D., van Laaten, M., . . . Burjánek, J. (2026). New research perspectives in light of dense cross-border experiments in west bohemia and vogtland regions. *Stud Geophys Geod*, *70*(23). doi: 10.1007/s11200-026-00025-6

Caron, M., Touvron, H., Misra, I., Jegou, H., Mairal, J., Bojanowski, P., & Joulin, A. (2021). Emerging properties in self-supervised vision transformers. In *2021 ieee/cvf international conference on computer vision (iccv)* (p. 9630-9640). doi: 10.1109/ICCV48922.2021.00951

Charles University in Prague, Institute of Geonics, Institute of Geophysics, Academy of Sciences of the Czech Republic, Institute of Physics of the Earth Masaryk University, & Institute of Rock Structure and Mechanics. (1973). *Czech regional seismic network.* International Federation of Digital Seismograph Networks. Retrieved from https://www.fdsn.org/networks/detail/CZ/ doi: 10.7914/SN/CZ

Dosovitskiy, A., Beyer, L., Kolesnikov, A., Weissenborn, D., Zhai, X., Unterthiner, T., ... Houlsby, N. (2020). An image is worth 16x16 words: Transformers for image recognition at scale. *CoRR*, *abs/2010.11929*. Retrieved from https://arxiv.org/abs/2010.11929

Fischer, T., Horálek, J., Hrubcová, P., Vavryčuk, V., Bräuer, K., & Kämpf, H. (2014). Intra-continental earthquake swarms in West-Bohemia and Vogtland: a review. *Tectonophysics*, *611*, 1–27. doi: 10.1016/j.tecto.2013.11.001

Heinicke, J., Stephan, T., Alexandrakis, C., Gaupp, R., & Buske, S. (2019). Alteration as possible cause for transition from brittle failure to aseismic slip: the case of the nw-bohemia / vogtland earthquake swarm region. *Journal of Geodynamics*, *124*, 79-92. doi: https://doi.org/10.1016/j.jog.2019.01.010

Hrubcová, P., Środa, P., Špičák, A., Guterch, A., Grad, M., Keller, G., ... Thybo, H. (2005). Crustal and uppermost mantle structure of the Bohemian Massif based on CELEBRATION 2000 data. *J. Geophys. Res.*, *110*, B11305. doi: 10.1029/2004JB003080

Institut fuer Geowissenschaften, Friedrich-Schiller-Universitaet Jena. (2009). *Thüringer seismologisches netz.* International Federation of Digital Seismograph Networks. Retrieved from https://www.fdsn.org/networks/detail/TH/ doi: 10.7914/SN/TH

Jiang, J., Stankovic, V., Stankovic, L., Murray, D., & Pytharouli, S. (2026). Generative self-supervised learning for seismic event classification. *Engineering Applications of Artificial Intelligence*, *165*, 113355. doi: https://doi.org/10.1016/j.engappai.2025.113355

Kasburg, V., Zehner, M., van Laaten, M., Müller, J., & Kukowski, N. (2025). Explainable seismic event discrimination: Improved explainability with vision transformers. *Journal of Geophysical Research: Machine Learning and Computation*, *2*(4), e2025JH000802. doi: https://doi.org/10.1029/2025JH000802

McInnes, L., Healy, J., & Melville, J. (2020). *Umap: Uniform manifold approximation and projection for dimension reduction.* Retrieved from https://arxiv.org/abs/1802.03426

Oquab, M., Darcet, T., Moutakanni, T., Vo, H., Szafraniec, M., Khalidov, V., ... Bojanowski, P. (2024). *Dinov2: Learning robust visual features without supervision.* Retrieved from https://arxiv.org/abs/2304.07193

Rimpot, J., Hibert, C., Malet, J.-P., Forestier, G., & Weber, J. (2025). Self-supervised learning based clustering workflow for exploring seismological data from dense networks. *Journal of Geophysical Research: Machine Learning and Computation*, *2*(4), e2025JH000958. doi: https://doi.org/10.1029/2025JH000958

Rimpot, J., Hibert, C., Retailleau, L., Saurel, J.-M., Malet, J.-P., Forestier, G., ... Pelleau, P. (2025). Self-supervised learning of seismological data reveals new eruptive sequences at the mayotte submarine volcano. *Geophysical Journal International*, *240*(1), 1-12. doi: 10.1093/gji/ggae361

Roy, O., & Vetterli, M. (2007). The effective rank: A measure of effective dimensionality. In *2007 15th european signal processing conference* (p. 606-610).

Ryan, E., Carbotte, S., Coplan, J., O'Hara, S., Melkonian, A., Arko, R., ... R., Z. (2009). Global multi-resolution topography (gmrt) synthesis data set. *Geochem. Geophys. Geosyst.*, *10*, Q03014. doi: 10.1029/2008GC002332

Siméoni, O., Vo, H. V., Seitzer, M., Baldassarre, F., Oquab, M., Jose, C., ... Bojanowski, P. (2025). *Dinov3.* Retrieved from https://arxiv.org/abs/2508.10104

Traag, V., Waltman, L., & van Eck, N. (2019). From louvain to leiden: guaranteeing well-connected communities. *Sci Rep*, *9*(5233). doi: 10.1038/s41598-019-41695-z van Laaten, M., & Wegler, U. (2024). Nonlinear inversion for a multilayer seismic s-wave attenuation model using radiative transfer theory. *Journal of Geophysical Research: Solid Earth*, *129*(8), e2023JB027989. doi: https://doi.org/10.1029/2023JB027989

van Laaten, M., Wegler, U., & Eulenfeld, T. (2023). On the trail of fluids in the northernmost intracontinental earthquake swarm areas of the Leipzig-Regensburg fault zone, Germany. *J. Seismol.*, *27*, 573–597. doi: 10.1007/s10950-023-10146-8

Vaswani, A., Shazeer, N., Parmar, N., Uszkoreit, J., Jones, L., Gomez, A. N., … Polosukhin, I. (2017). Attention is all you need. *CoRR*, *abs/1706.03762*. Retrieved from `http://arxiv.org/abs/1706.03762`

Zhou, J., Wei, C., Wang, H., Shen, W., Xie, C., Yuille, A. L., & Kong, T. (2021). ibot: Image BERT pre-training with online tokenizer. *CoRR*, *abs/2111.07832*. Retrieved from `https://arxiv.org/abs/2111.07832`

Table 1. Data-driven macro-classes obtained by grouping the 32 Leiden clusters, with approximate window counts and interpretation. Counts sum to ≈198,000. Temporal signatures are read from Figures 8!!! and 9!!! and use no catalogue labels.

Macro-class	Windows	Example clusters	Temporal signature	Interpretation
Earthquake (tectonic)	21,400	C7, C17, C23, C25, C27	Flat by weekday and hour	Swarm and isolated local earthquakes
Teleseismic	500	C31	Sparse, no diurnal pattern	Distant large earthquakes (Section 4.5)
Quarry blast	30,500	C4, C8, C10, C22	Mon-Fri, midday peak	Anthropogenic surface blasts
Transient (ambient)	102,200	C0, C1, C2, ...	Weekend-elevated, daytime	Weather/ambient transients
Noise	22,600	C3, C29, C30	Weekend-elevated, night	Background and instrumental noise
Instrument & machinery	6,800	C16, C30	Weekday, midday	Machinery, traffic, monochromatic instrument lines
Artifact & episode	5,900	C18	2023 episode	Data-quality episode
Mixed	8,400	-	Weekday, midday	Overlapping or ambiguous windows

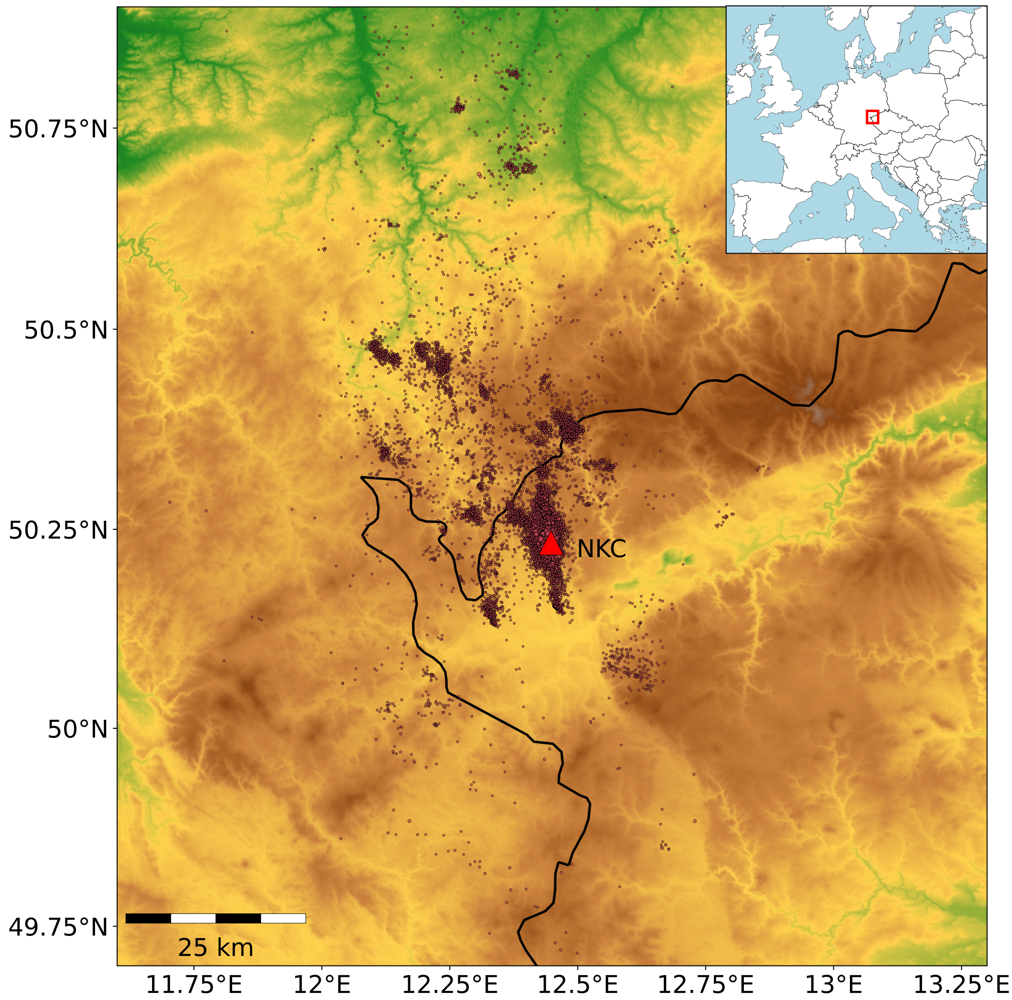

Figure 1. Map view of the study area, with the topography coloured. The station NKC is marked as red triangle and the catalogued seismicity as dots. The thick line marks the Czech–German border and the inset locates the region in central Europe.

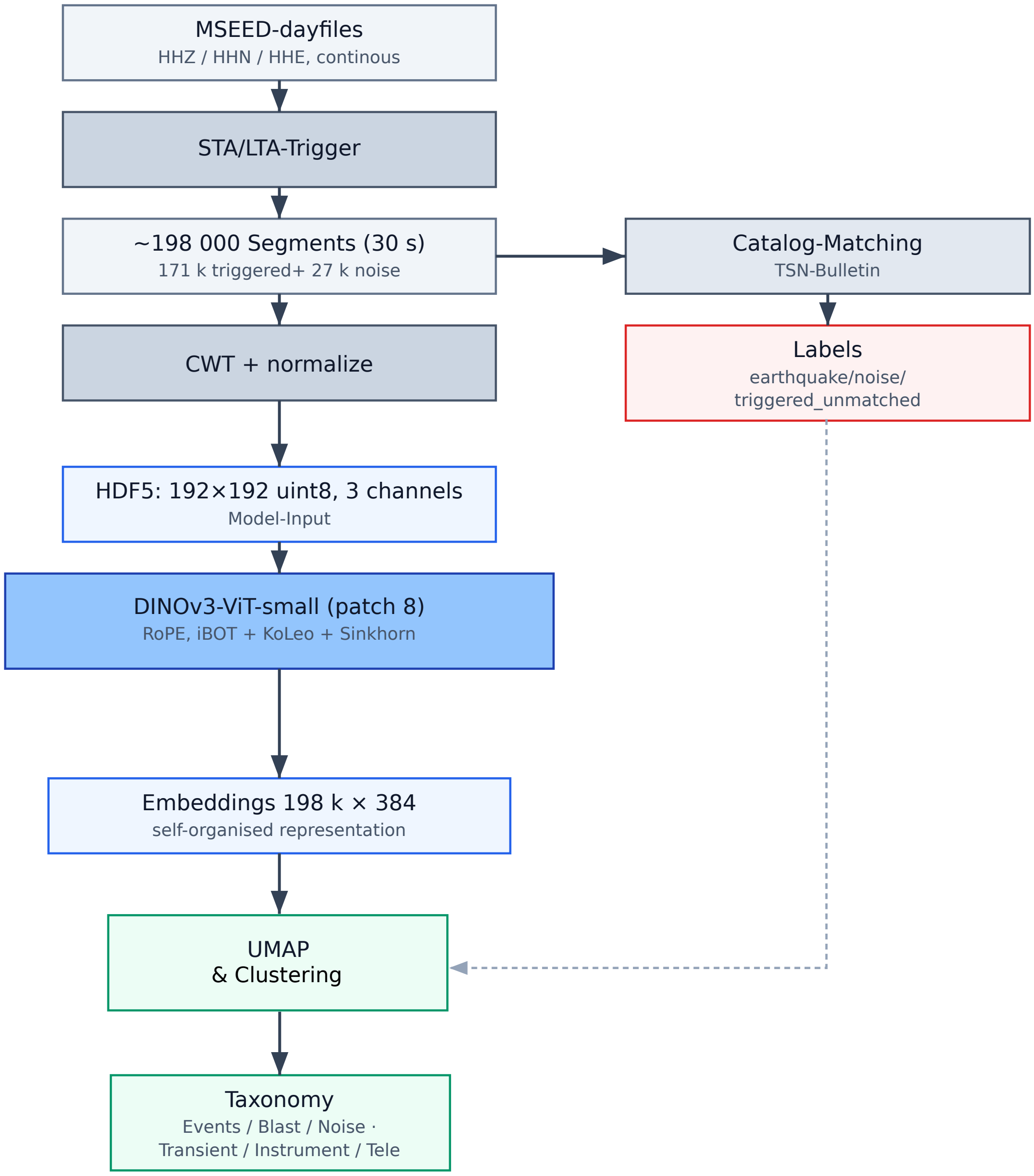

Figure 2. Processing pipeline. Continuous three-component recordings (HHZ/HHN/HHE) are STA/LTA-triggered into ≈198,000 windows of 30 s. Each window is transformed to a three-channel CWT spectrogram, normalised, and stored as a 192 × 192 8-bit image. A DINOv3 ViT-small (patch 8) with RoPE, iBOT, KoLeo, and Sinkhorn–Knopp centring produces a 198,000 × 384 self-organised embedding, which is projected with UMAP and clustered (Leiden) into a taxonomy. Catalogue matching against the TSN bulletin (dashed path) supplies reference labels for evaluation only.

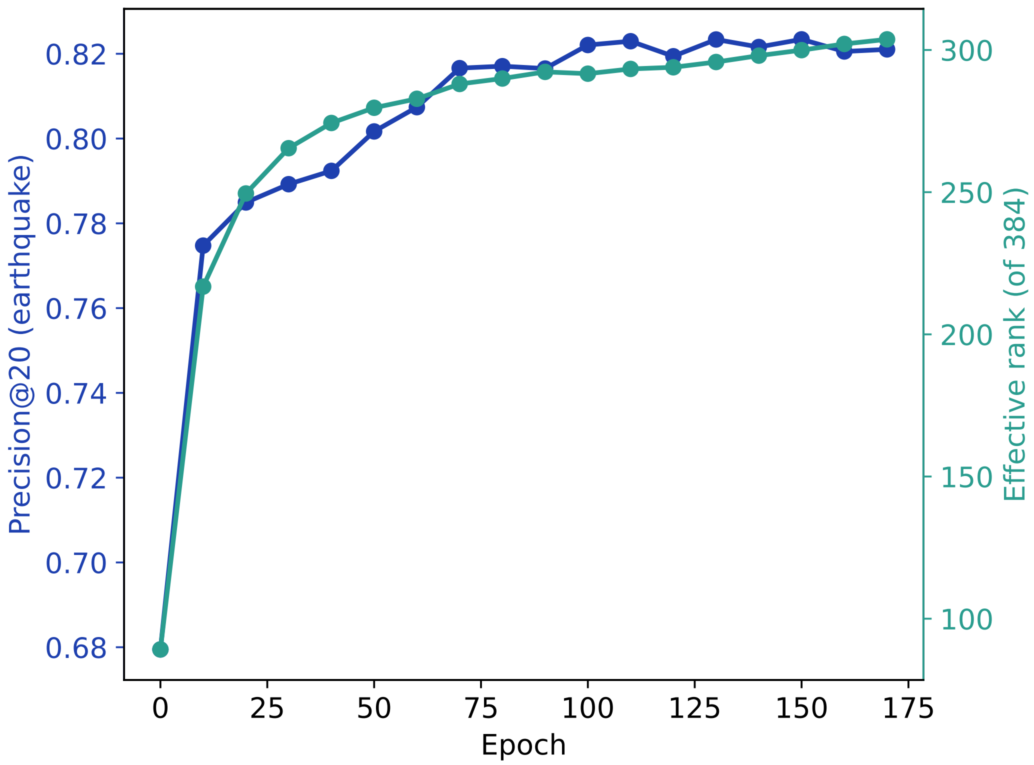

Figure 3. Training diagnostics. Earthquake retrieval precision P@20 (blue, left axis) and the effective rank of the embedding (green, right axis, out of 384) as a function of training epoch. Both rise together and plateau. The effective rank increases monotonically, indicating no representational collapse.

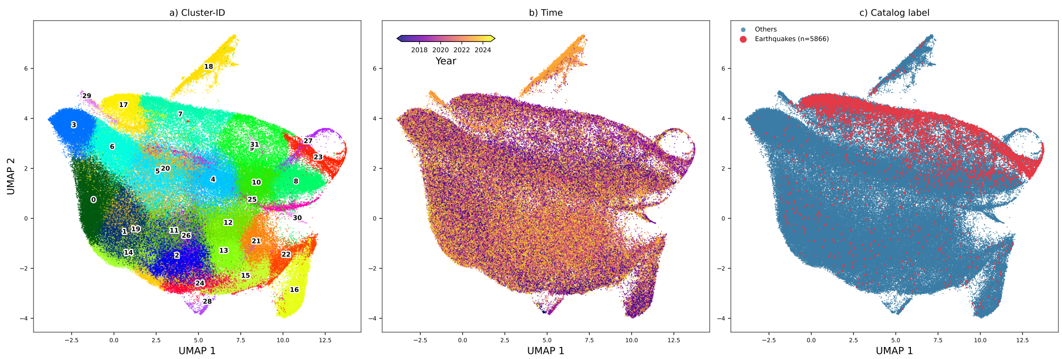

Figure 4. UMAP projection of the learned representation, coloured a) by Leiden cluster, b) by year, and c) by catalogue label, with catalogue earthquakes (n = 5,866 windows) in red and all other windows in blue. Earthquakes occupy a coherent, well-separated region of the map.

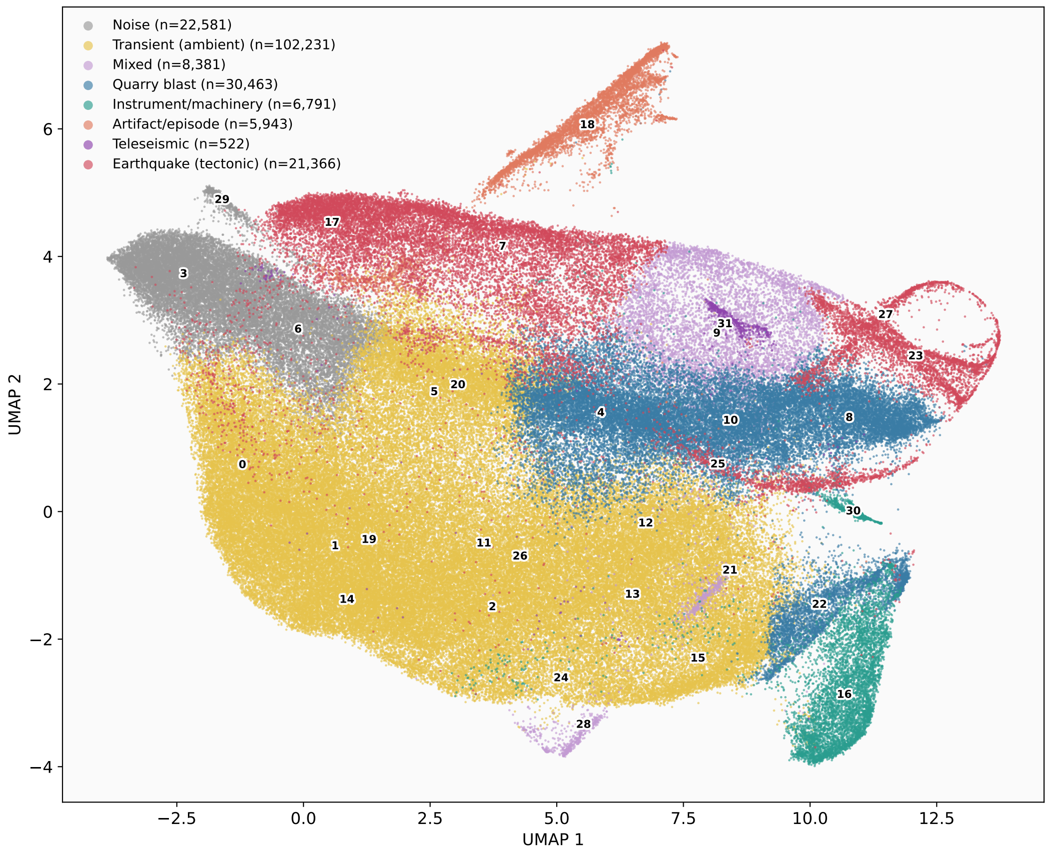

Figure 5. The same UMAP projection coloured by the eight data-driven macro-classes of Table 1, with per-class window counts. The ambient-transient class forms the central bulk, earthquakes, quarry blasts, and the smaller classes occupy distinct territories.

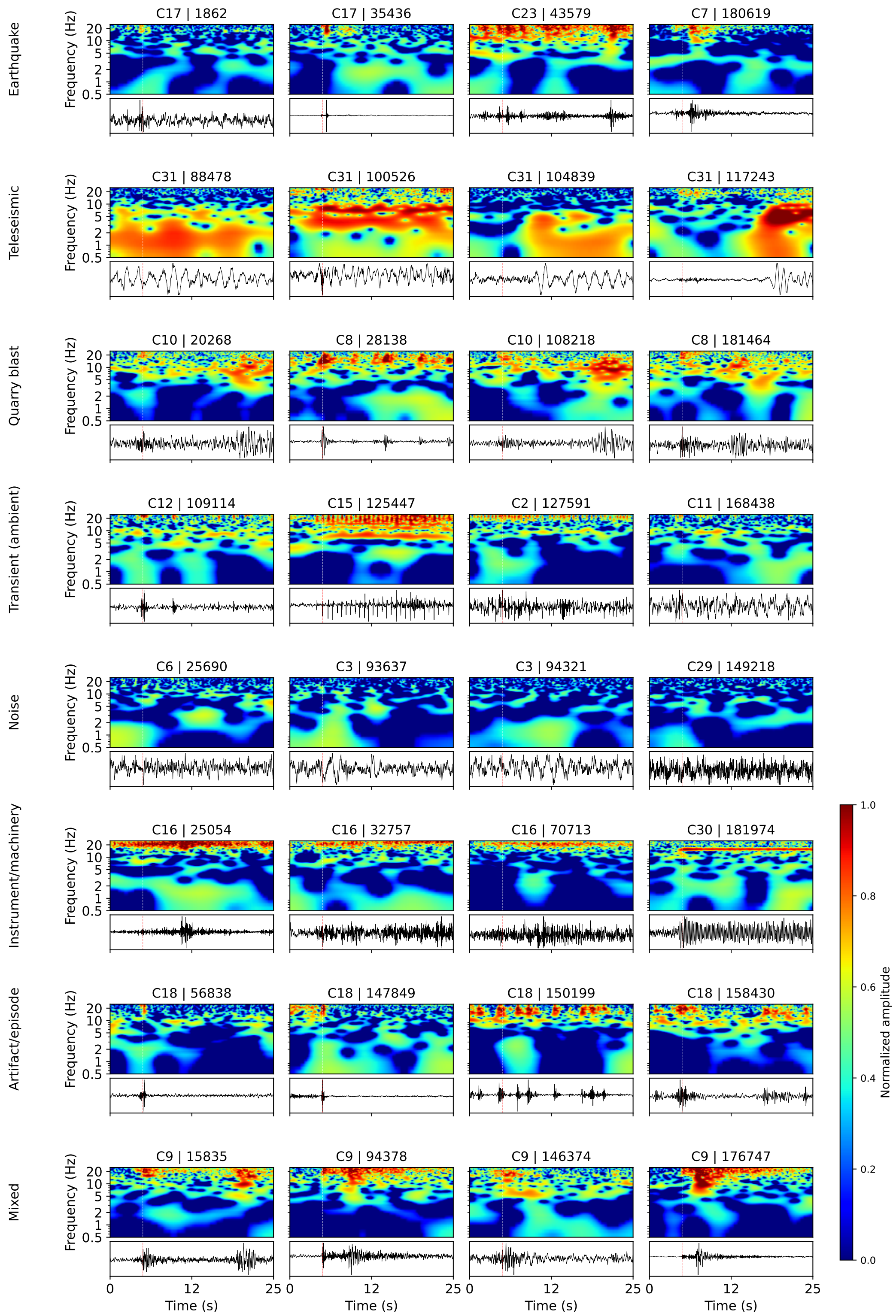

Figure 6. Examples of events clustered in each of the macro-classes.

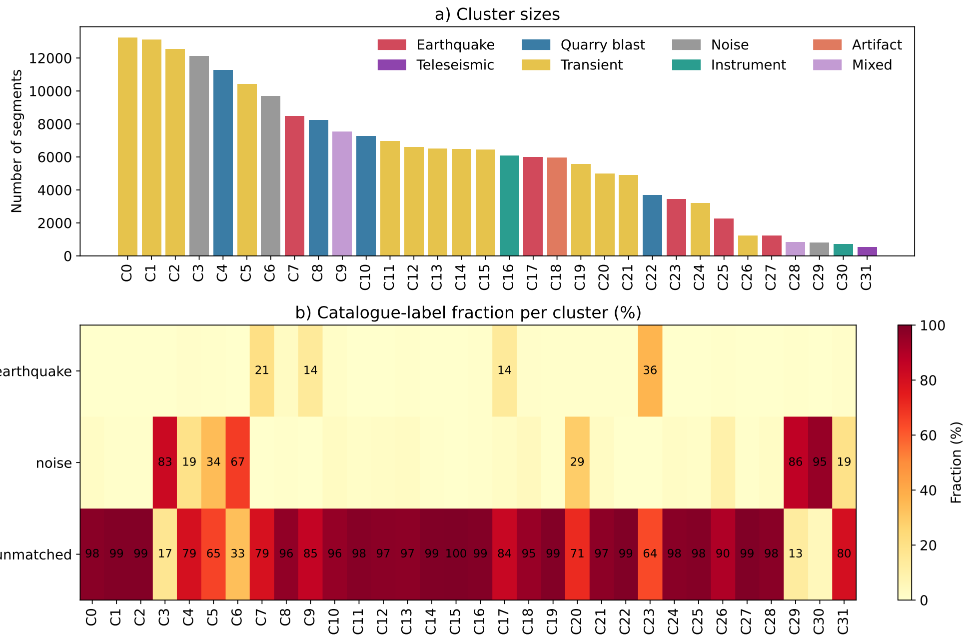

Figure 7. Cluster sizes and composition. a) The 32 Leiden clusters ordered by number of windows, coloured by macro-class. b) Fraction of each cluster carrying the earthquake, noise, and triggered unmatched reference labels. The triggered unmatched label dominates most clusters, including the earthquake-enriched ones.

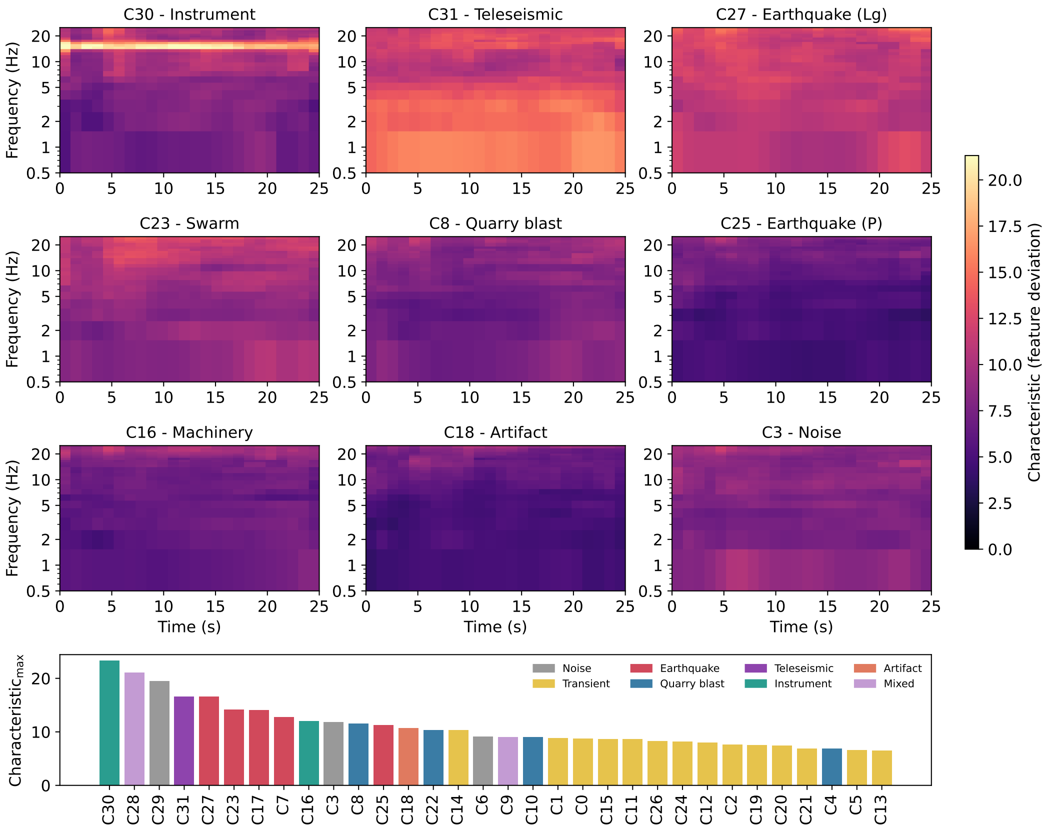

Figure 8. Feature-deviation signatures. Time–frequency maps of the mean patch-feature deviation for nine representative clusters, showing the physical identity of the distinctive classes (e.g., a monochromatic instrument line at approx. 15 Hz in C30, broadband low-frequency energy in the teleseismic cluster C31, quarry-blast and machinery signatures in C8 and C16, P- and Lg-dominated earthquake signatures in C25 and C27). Bottom: Characteristic$_{\mathrm{max}}$ for all 32 clusters, coloured by macro-class. Distinctive clusters reach 12–23 while the ambient-transient bulk stays at 7–9, indicating over-fragmentation of the bulk.

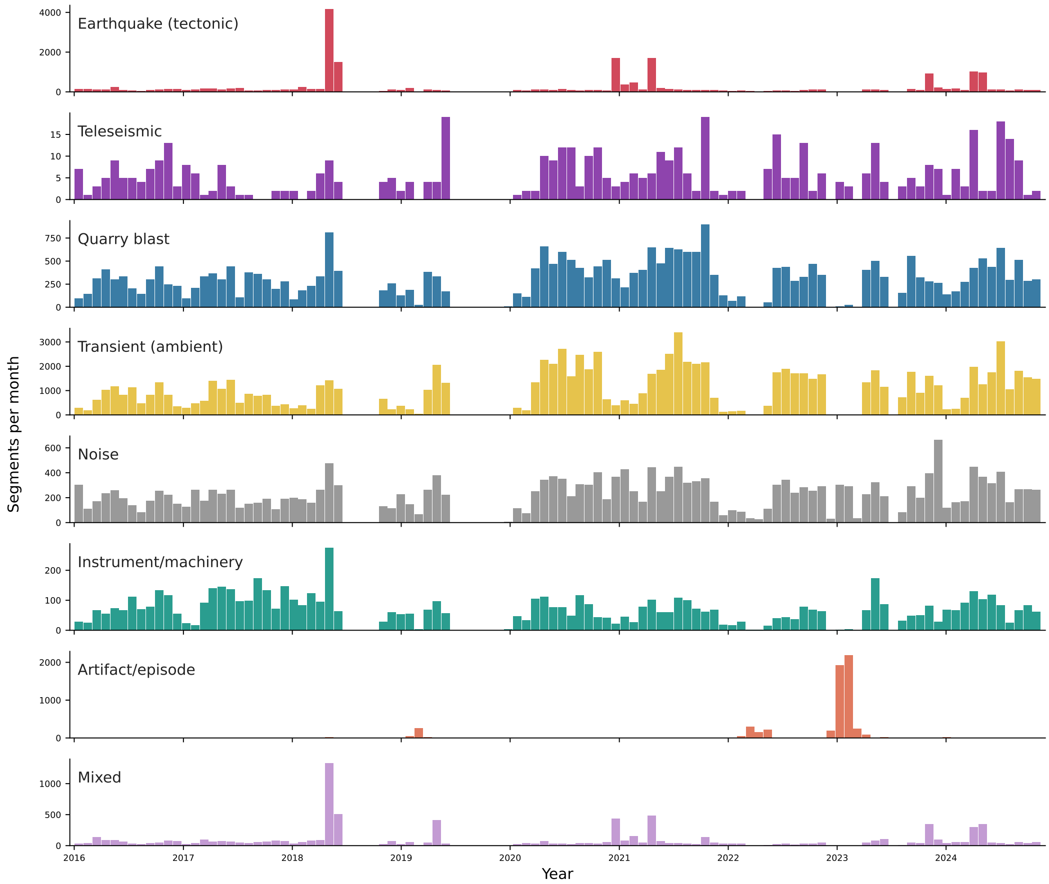

Figure 9. Monthly window counts per macro-class over 2016-2024. The earthquake class peaks in the documented swarm episodes (prominently around 2018, with further episodes around 2021 and 2024), the artifact/episode class is concentrated in a single 2023 data-quality episode.

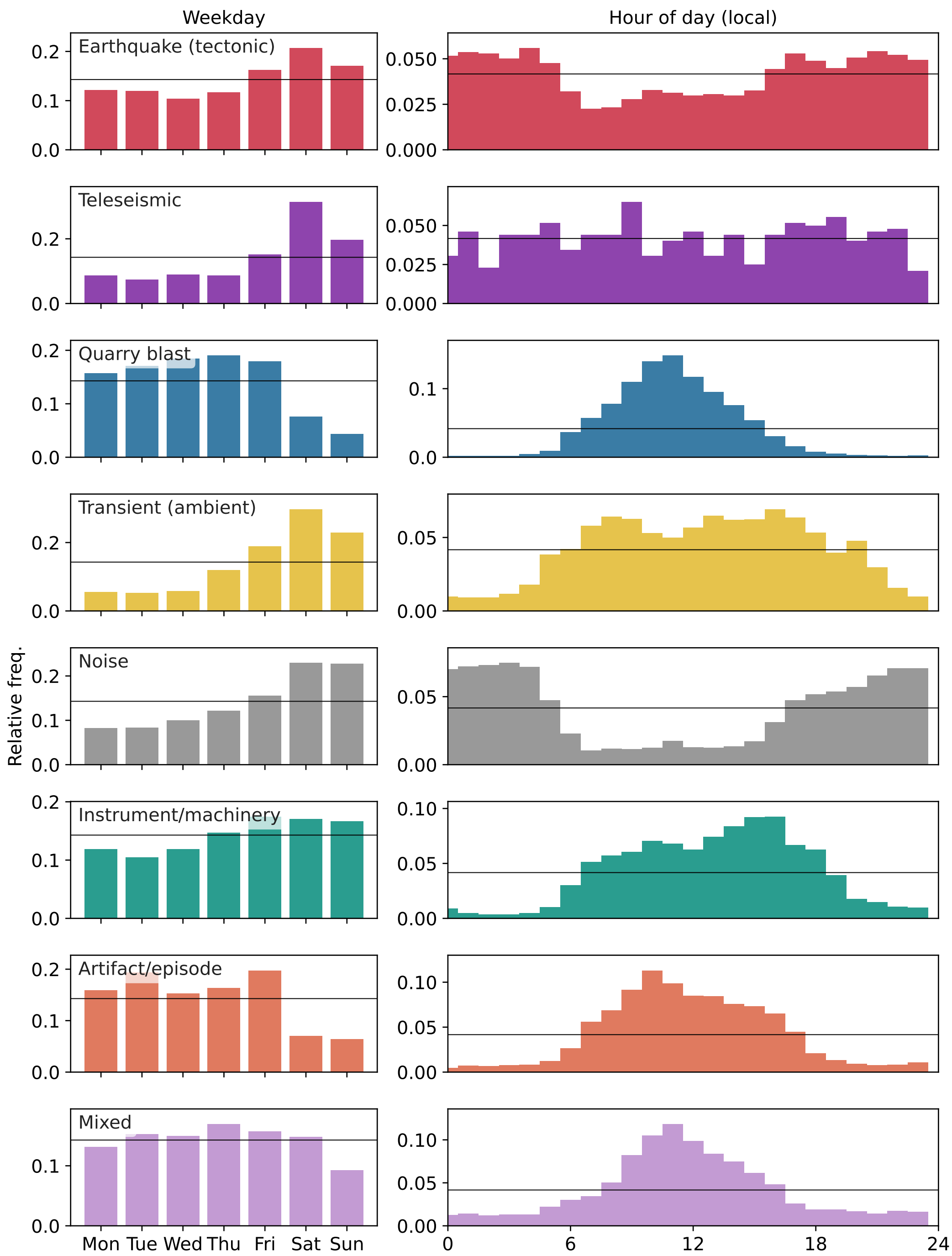

Figure 10. Relative frequency of each macro-class by weekday (Mon–Sun) and by hour of day (local). Quarry blasts concentrate on working days and around midday; earthquakes are flat; ambient transients and noise are weekend-elevated. Horizontal lines mark the uniform expectation. Computed from time stamps alone.

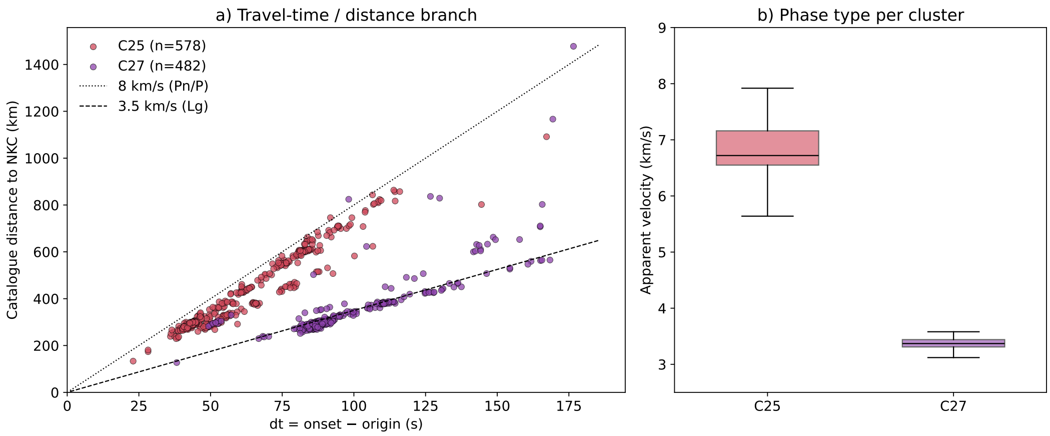

Figure 11. Earthquake phase sub-structure. a) Delay between catalogued origin time and window onset versus catalogued epicentral distance for the two earthquake clusters C25 (n = 578) and C27 (n = 482), with reference lines at 8 km/s (P/Pn) and 3.5 km/s (Lg). b) Apparent-velocity distributions for the two clusters. C25 follows the fast P/Pn branch and C27 the slow Lg branch, showing that the representation separates earthquake windows by dominant phase.